Quasifree mechanism in the Li-6 + Li-6 → 3α reaction at low energy

Spitaleri, C.; Tumino, A.; Lattuada, M.; Pizzone, R.G.; Tudisco, S.; Miljanić, Đuro; Blagus, Saša; Milin, Matko; Skukan, Natko; Soić, Neven

Source / Izvornik: **Physical Review C - Nuclear Physics, 2015, 91**

Journal article, Published version
Rad u časopisu, Objavljena verzija rada (izdavačev PDF)

https://doi.org/10.1103/PhysRevC.91.024612

Permanent link / Trajna poveznica: https://urn.nsk.hr/urn:nbn:hr:217:049817

Quasifree mechanism in the ^{6}Li + ^{6}Li → 3α reaction at low energy

C. Spitaleri,[1,2,*] A. Tumino,[1,3] M. Lattuada,[1,2] R. G. Pizzone,[1] S. Tudisco,[1] Đ. Miljanić,[4] S. Blagus,[4] M. Milin,[5] N. Skukan,[4] and N. Soić[4]

[1]*INFN, Laboratori Nazionali del Sud, I-Catania, Italy*
[2]*Dipartimento di Fisica e Astronomia, Universitá di Catania, I-Catania, Italy*
[3]*Facoltá di Ingegneria e Architettura, Universitá degli Studi di Enna "Kore", I-Enna, Italy*
[4]*Ruđer Bošković Institute, Zagreb, Croatia*
[5]*Faculty of Science, University of Zagreb, Zagreb, Croatia*

(Received 4 December 2014; published 18 February 2015)

The ^{6}Li + ^{6}Li → 3α reaction was measured in a kinematically complete experiment at 3.1 and 2.5 MeV to investigate the presence of quasifree processes at sub-Coulomb energies. Results from the present experiment show a very clear evidence of quasifree mechanisms with an α-particle spectator either in the target or in the projectile. To check the occurrence of quasifree processes, "energy sharing" and "angular correlation" analyses have been performed in the framework of the plane wave impulse approximation, both leading to consistent results. The huge peak in the angular correlation spectra, previously ascribed to the "anomalous quasifree" process, corresponds instead to the population of the 22.2-MeV (2^+, Γ = 800 keV) state of ^{8}Be.

DOI: 10.1103/PhysRevC.91.024612 PACS number(s): 25.70.Mn, 24.50.+g, 24.30.−v

I. INTRODUCTION

In previous years, the ^{6}Li + ^{6}Li → 3α reaction around the Coulomb barrier was experimentally investigated by several authors [1–14], in several cases for astrophysical studies via the Trojan Horse method [15–22]. Both sequential decay (SD) through ^{8}Be excited states and direct processes were seen to contribute to the reaction cross section. Such direct contributions have been mainly interpreted as from quasifree (QF) processes, in which an α cluster, either in the target or in the projectile, is spectator of the ^{6}Li+d → 2α virtual reaction. The two QF processes, referred to as quasifree reactions in the target $(\mathrm{QFR})^t$ and in the projectile $(\mathrm{QFR})^p$ show cross-section enhancements in the α-α energy and angular correlations. These results were obtained by Gadeken and Norbeck [8] at 6 MeV and 13 MeV incident energy. Their data were fitted by plane wave Born approximation (PWBA) calculations. They also found that at 2 MeV of beam energy events did not fall in the two kinematical regions corresponding to QF processes, but rather in an intermediate one providing a huge peak in the α-α angular correlation spectra. This effect was interpreted [10,11] as due to the long-range Coulomb interaction which slows down the relative motion of the two ^{6}Li nuclei. The two ^{6}Li would interact only after they are stopped by the Coulomb repulsion and the two standard QF processes are no longer distinguishable.

A set of measurements of α-α energy and angular correlation was performed at incident energies between 3 and 7 MeV to investigate the transition from quasifree regime $(\mathrm{QFR})^t$ and $(\mathrm{QFR})^p$ to the so-called "anomalous quasifree" (AQF) effect. This systematics is reported in Ref. [14].

While PWBA could not describe such a process, the introduction of a distorted wave Born approximation (DWBA) treatment was successful in reproducing the height of the huge peak at 2 MeV [10,14], but not the shape of the distribution, with the tails falling below two mild enhancements shown in Ref. [14]. These tentative structures may belong to the two QF processes. This has triggered a new higher resolution experimental work on the ^{6}Li + ^{6}Li → 3α reaction thanks to the advances in the detection systems and electronic devices available today and to the more sophisticated event-by-event data analysis available nowadays. The present paper reports a new measurement performed at 3.1 and 2.5 MeV of beam energy. The aim was to investigate the existence of QF processes at such low energy that from kinematics appear well separated. Two steps were employed in the analysis of experimental data: first "energy sharing" (ES) and "angular correlation" (AC) analysis was performed to check the existence of the QF mechanisms, then a new interpretation of the huge peak in the α-α angular correlation spectra based on the population of the 22.2-MeV state of ^{8}Be is suggested.

II. THE EXPERIMENT

The ^{6}Li + ^{6}Li → 3α experiment was performed using the EN Tandem Van de Graaff accelerator of the Ruđer Bošković Institute in Zagreb. A 3.1- and 2.5-MeV ^{6}Li^{++} Tandem beam with intensity of about 3 nA, was delivered onto an isotopically enriched ^{6}LiF target, 87-μg/cm^2 thick, evaporated on a carbon backing, 27-μg/cm^2 thick. The beam spot was reduced to 2 mm in diameter using a collimation system. The beam energies at half target were 2.73 and 2.11 MeV for the 3.1 and 2.5 MeV runs, respectively. All further calculations were performed using the beam energies at half target. The experimental setup consisted of four single area, 1000-μm position sensitive detectors (PSD), 50 × 10 mm^2 in a coplanar geometry on both sides of the beam direction. The α-α coincidences were measured by any two of the PSD's placed on opposite sides with respect to the beam direction. Positions, distances, solid angles, and other characteristics of the detectors are listed in Table I.

*spitaleri@lns.infn.it

TABLE I. Information on the detector geometry: central angle θ_L, angular coverage $\Delta\theta_L$, distance from target d, solid angle $\Delta\Omega$, and thickness s.

Det.	θ_L (degree)	$\Delta\theta_L$ (degree)	d (mm)	$\Delta\Omega$ (msr)	s (μm)
PSD_1	107	94–121	110	41.3	1000
PSD_2	60	52–68	200	12.5	1000
PSD_3	−60	−52 to −68	200	12.5	1000
PSD_4	−81	−74 to −98	110	41.3	1000

This setup allowed us to investigate all kinematical conditions for which the spectator momentum $p_s^{(t)}$ (in the target) or $p_s^{(p)}$ (in the projectile), is zero. Indeed, the cross section for QF processes is expected to have maxima for these kinematical conditions, because the α-d intercluster motion in ^{6}Li is known to be mainly in an S state. Denoting by $\mathbf{p_0}$ the momentum of the incoming ^{6}Li and by $\mathbf{p_3}$ the momentum of the undetected third α particle, the spectator momentum is given by

(i) $p_s^{(t)} = p_3$ spectator in the target.
(ii) $p_s^{(p)} = p_3$-$2/3p_0$ spectator in the projectile.

Examples of expected detection angles for the two cases in which the spectator is left with zero momentum are reported in Table II. These angles are called quasifree angles. No particle identification technique was used during the experiment, because the Q value (20.899 MeV) for the ^{6}Li(^{6}Li,$\alpha\alpha$)^{4}He reaction, is the largest among the other possible three-body reactions occurring on lithium, fluorine, carbon, oxygen, and other impurities in the target. The choice of the detection angles was determined according to the three-body kinematics for emission of two α particles in the assumption of the quasifree process either in the target or in the projectile.

We are therefore interested in coincidence events between PSD_1 and PSD_3 for $(QFR)^p$ and PSD_2 and PSD_4 for $(QFR)^t$. We will refer in the following to them as coincidences C_{13}, C_{24}, respectively.

The angular ranges covered by the detectors correspond to momentum values of undetected α particle ranging from about −200 MeV/c to about 200 MeV/c for both QF processes. This assures that the bulk of the QF contribution for the process of interest lies inside the investigated region. This allowed one also to cross-check the method inside and outside the phase-space regions where the QF contribution is expected.

TABLE II. Examples of quasifree angles in the $(QFR)^t$ and $(QFR)^p$ at 2.73(3.1) and 2.11(2.5) MeV, respectively.

θ_2(deg)	Spectator in target θ_1(deg) 2.73 MeV 2.11 MeV	Spectator in projectile θ_1(deg) 2.73 MeV 2.11 MeV
57	90.1 94.1	112.6 113.9
60	86.6 90.6	109.3 110.7
63	83.2 87.2	106.1 107.4

The energy and position signals of each PSD were processed by standard electronics together with the delay between the time signals coming from any two PSD's. In preliminary runs of the measurements, masks with 18 equally spaced slits were placed in front of each PSD to perform position calibration. Energy calibration was performed using the $^6\text{Li} + {}^{12}\text{C} \rightarrow \alpha + {}^{14}\text{N}$ reaction at 8 MeV. Moreover, a three-peak α source (^{239}Pu, ^{241}Am, ^{244}Cm) was used for low-energy calibration.

An overall energy resolution better than 1% and angular resolution of about 0.5° were obtained. The beam spot size and energy spread were taken into account, as well as the energy loss in the target and in the dead layers of the detectors.

III. SELECTION OF THE 3-α CHANNEL

A number of steps are needed in the data analysis before the experimental momentum distribution can be extracted. These steps include the identification of events from the three-body reaction of interest $^6\text{Li} + {}^6\text{Li} \rightarrow 3\alpha$, the separation of the contributions from different reaction mechanisms, and the selection of the related events.

Data analysis was performed for the full body of coincidence events from the two runs at 3.1 and 2.5 MeV separately, providing consistent results. To discuss the different steps, only figures for the 3.1-MeV run will be shown, because more than 80% of statistics of the experiment comes from this run. As known, in a reaction with three bodies in the exit channel, two-dimensional plots between the energies of any two of the involved particles show their correlation in terms of energy and momentum conservation. Thus, they can be used to select the reaction channel of interest. A typical energy correlation plot obtained from the detected particles is shown in Fig. 1 for coincidence C_{24}. Events corresponding to the $^6\text{Li} + {}^6\text{Li} \rightarrow 3\alpha$

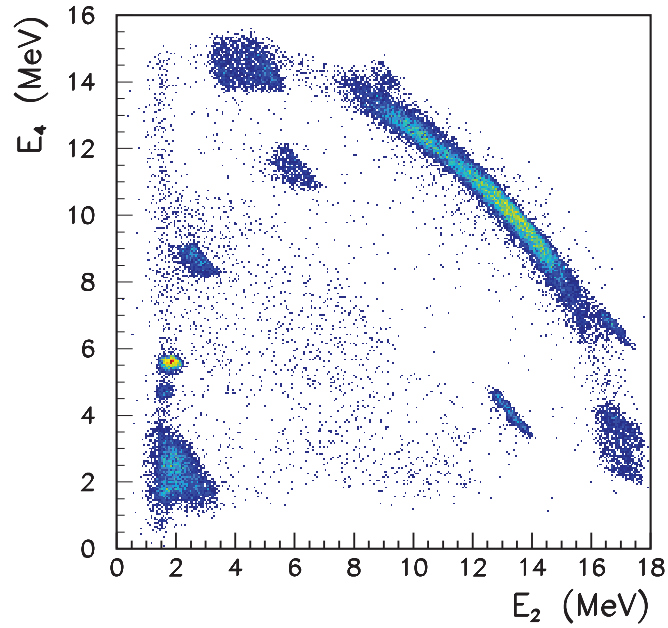

FIG. 1. (Color online) Energy correlation plot from the detected particles for coincidence C_{24}.

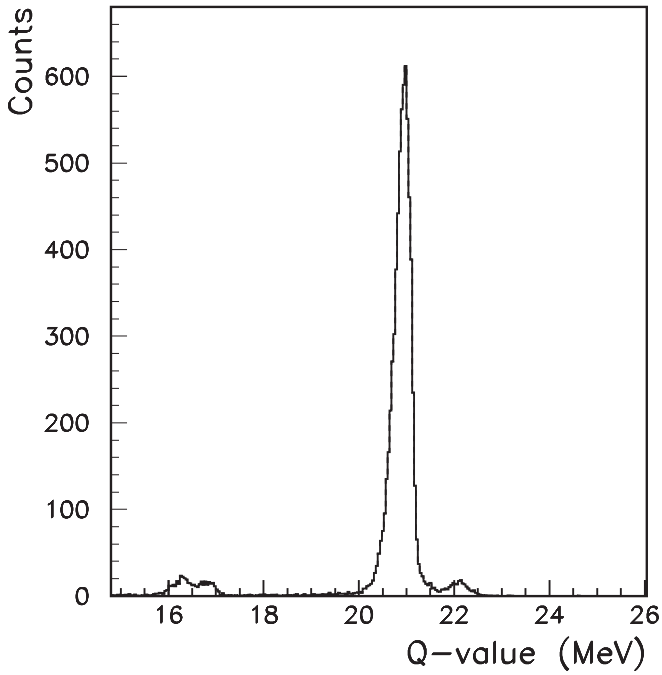

FIG. 2. Q-value spectrum for coincidence C_{24}. The sharp peak around 20.9 MeV, corresponds to the ^{6}Li + ^{6}Li → 3α reaction.

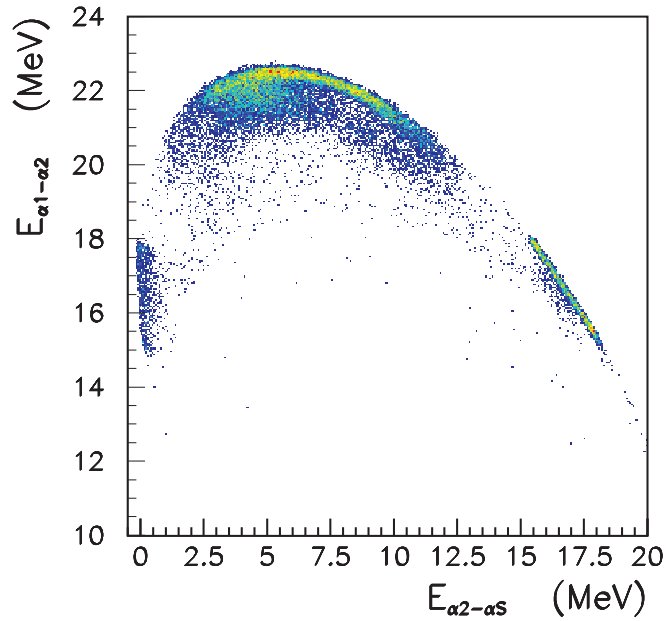

FIG. 3. (Color online) $E_{\alpha_1\alpha_2}$ vs $E_{\alpha_2\alpha_S}$ relative energy scatter plots for coincidence events at 3.1 MeV of beam energy (coincidence C_{24}).

reaction were singled out from comparison with a Monte Carlo simulation of the process, which accounts for the experimental and kinematics constraints. Side events appearing as spots correspond mostly to binary reactions that represent an easily removable background. Indeed, in the present experiment only two of the three emitted particles were detected and the reaction channel of interest was reconstructed under the assumption of a third α as undetected particle. This technique does not introduce any ambiguities in the present case, because the Q value (20.899 MeV) for the ^{6}Li + ^{6}Li → 3α reaction is much larger than that of other possible reactions occurring on carbon backing or impurities in the target. The Q-value spectrum for coincidence C_{24} is reported in Fig. 2. The spectrum shows a prominent peak at about 20.9 MeV in very good agreement with the expected value. Similar results were obtained for coincidence C_{13}. The small peaks on the left side are attributed to the ^{6}Li + ^{7}Li → ^{9}Be + ^{4}He (from 5% contaminant ^{7}Li) and ^{6}Li + ^{12}C → ^{14}N + ^{4}He (from carbon backing) two-body reactions while the one on the right side corresponds to ^{6}Li + ^{6}Li → ^{8}Be + ^{4}He. However, their Q values are wrongly reconstructed because all events are treated as they would belong to a reaction with three bodies in the exit channels. Notwithstanding, they show up as peaks/spots that can be easily separated from the prominent 3α channel. Events inside the Q-value peak at 20.9 MeV were selected for further analysis.

After the selection of the ^{6}Li + ^{6}Li → 3α reaction channel, the next step of data analysis is to examine if, in the considered kinematic regions, the contribution of the quasifree process to the overall α-α coincidence yield is evident and well separated from others. The analysis of the experimental results is in general complicated by the presence of other reaction mechanisms, such as sequential decays, producing the same three α particles in the final state.

To study the nature of the events belonging to the ^{6}Li + ^{6}Li → 3α reaction, relative energies for any two of the three final α particles were obtained for C_{13} and C_{24} coincidences. In the following, the detected α particles from any of the selected coincidences will be indicated with symbols α_1 (particle detected in PSD1 or PSD4) and α_2 (particle detected in PSD3 or PSD2), while α_S will stand for the undetected α particle. In QF events α_S will be the spectator particle. The scatter plot for relative energies $E_{\alpha_1\alpha_2}$ vs $E_{\alpha_2\alpha_S}$ is shown in Fig. 3 as an example. Similar results were obtained for coincidence C_{13}. In these plots, any event correlation appearing as a horizontal or vertical or bended line, gives evidence of the formation of an excited intermediate ^{8}Be, finally decaying into two α's. From this representation there is evidence of correlation corresponding to the ground state of ^{8}Be and mildly to the doublet at 16.6 and 16.9 MeV and to the 3.03-MeV state although affected by the limited phase space populated in the experiment. In addition, a strong contribution in the region of the 22.2-MeV state of ^{8}Be is apparent in the $E_{\alpha_1\alpha_2}$ variable. However, the evidence of correlation is smoothed by the phase space cutoff at 22.3 MeV (sum of Q value and center-of-mass beam energy) that allows only half of this state (800 keV total width) to be populated. Nonetheless, even half of the total contribution is anything but negligible. From kinematics, QF events are expected to contribute right below $E_{\alpha_1\alpha_2} = 22$ MeV, in a region where sequential decays from the ^{8}Be states at 3.03 (in $E_{\alpha_1\alpha_S}$ and $E_{\alpha_2\alpha_S}$), 22.2 (in $E_{\alpha_1\alpha_2}$) and possibly 19.9–20.3 MeV (in $E_{\alpha_1\alpha_2}$), can play a role. To perform a correct selection, ES and AC analysis are required as described in the following.

IV. BASIC FEATURES OF THE QUASIFREE MECHANISM

To facilitate the understanding of the measurements and to better explain the nuclear reaction mechanisms that are

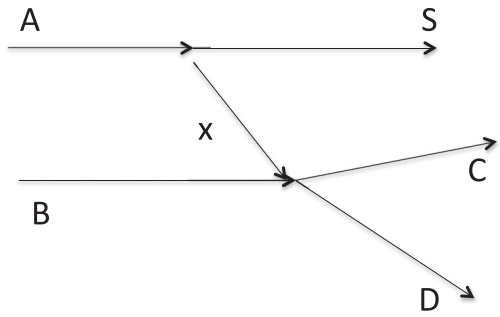

FIG. 4. Diagram representing the quasifree $B(A,C\ D)S$ process; particle B interacts only with cluster x, leaving S as spectator to the process.

involved in the ^{6}Li(^{6}Li,$\alpha\alpha$)^{4}He reaction at these low energies, a brief presentation of the basic theory of the QF mechanism is given here.

In general, the quasifree $A + B \rightarrow C + D + S$ reaction can be described by means of the pole diagram shown in Fig. 4, where only the first term of the Feynman series is retained [23,24]. If a suitable selection of quasifree events is performed, this diagram represents the dominant process (pole approximation), while other graphs (triangle graphs) indicating rescattering between the reaction products, are negligible [23–25]. This process can be described as a transfer to the continuum, in which the nucleus A breaks up into the transferred cluster x (participant) and the cluster S acting as a spectator to the $x + B \rightarrow C + D$ virtual reaction. The nucleus A should have a strong $x + S$ cluster structure to maximize the QF yield.

The theory of direct reactions [42] is the theoretical background to the study of the QF reaction mechanisms.

The QF study is performed in plane wave impulse approximation (PWIA) as well as in distorted wave impulse approximation (DWIA). In both approximations without spin-orbit-dependent distortions, the three-body reaction cross section is proportional to the cross section of the virtual two-body reaction [see Eq. (1)] [23–25].

Following the simple PWIA, the three-body reaction cross section can be factorized into two terms corresponding to the two vertices of Fig. 4 and it is given by [26]

$$\frac{d^3\sigma}{d\Omega_C d\Omega_D dE_C} = P(\mathrm{KF})\phi(p_S)^2 \times \left[\frac{d\sigma}{d\Omega}\right]^{\mathrm{HOES}}_{x+B\rightarrow C+D}, \quad (1)$$

where

(i) P is the factor that takes into account clustering probability and/or absorption effects.

(ii) $[\frac{d\sigma}{d\Omega}]_{x+B\rightarrow C+D}$ is the half-off-energy-shell (HOES) differential cross section for the binary $B(x,C)D$ reaction at the center-of-mass energy $E_{\mathrm{c.m.}}$ given in postcollision prescription by [5]

$$E_{\mathrm{c.m.}} = E_{CD} - Q_{2b}, \quad (2)$$

where Q_{2b} is the Q value of the binary $x + B \rightarrow C + D$ reaction and E_{CD} is the $C - D$ relative energy in the exit channel.

(iii) KF is a kinematical factor containing the final state phase space factor and it is a function of masses, momenta, and angles of the detected particles.

(iv) $\phi(p_S)^2$ is the square of the Fourier transform of the radial wave function for the $x - S$ intercluster motion usually described in terms of Hankel, Eckart or Hulthn functions depending on the properties of the $x - S$ system.

In the present case, the validity conditions of the impulse approximation (IA) have been checked [27]. The high Q value (20.9 MeV) of the ^{6}Li(^{6}Li,$\alpha\alpha$)^{4}He implies that a ^{6}Li incident energy of 3.1 MeV (2.5 MeV) corresponds to a quite high Galilean invariant transferred momentum q_t of about 280 MeV/c (275 MeV/c) [27–29] and to an associated de Broglie wavelength $\lambda = 4.3$ (4.4) fm, small enough with respect to the ^{6}Li effective radius of about 6 fm [28]. Thus, the IA is suitable for the description of the process.

The determination of the HOES differential cross section in absolute units is subjected to the knowledge of P [30], which is usually far from being easily and accurately fixed, because, for example, of the large errors affecting the spectroscopic factors. Nonetheless, this is not a limit because the normalization can be obtained from direct data when necessary [22].

The region where the pole diagram is expected to be dominant is fixed by [23,24]

$$0 \leqslant p_S \leqslant K_S, \quad (3)$$

with K_S the OES wave number [24], given by

$$K_S = \sqrt{2\mu_{xS}B_{xS}}, \quad (4)$$

where μ_{xS} and B_{xS} are the reduced mass and the binding energy of the $x - S$ system, respectively.

V. EXPERIMENTAL EVIDENCE OF THE QUASIFREE MECHANISM

A. Energy sharing analysis for (QFR)^p and (QFR)^t

To disentangle the QF coincidence data from the SD contribution fed by excited states of ^{8}Be, the following procedure based on the ES methodology was employed. The first step was to select kinematic regions where the QF mechanism contribution is expected to dominate, i.e., around the QF angles. Coincidence events for each pair of QF angles from both projectile and target breakups, were then projected onto the E_1 (E_4), E_3 (E_2), and $E_{\alpha_1\alpha_2}$ axes. Note that the two projections are not strictly equivalent because of the broadening of the kinematical locus from the experimental effects. Typical results are shown in Fig. 5 (energy spectrum in the E_1 variable), and Fig. 6 ($E_{\alpha_1\alpha_2}$ spectrum) for (QFR)^p at the QF angles $\theta_1 = 109.3^\circ \pm 1^\circ$ and $\theta_3 = 60^\circ \pm 1^\circ$, and in Fig. 7 (energy spectrum in the E_4 variable), and Fig. 8 ($E_{\alpha_1\alpha_2}$ spectrum) for (QFR)^t at the QF pair $\theta_4 = 86.5^\circ \pm 1^\circ$ and $\theta_2 = 60^\circ \pm 1^\circ$. The upper part of each energy spectrum shows the corresponding calculated $E_{\alpha_1-\alpha_2}, E_{\alpha_1-\alpha_S}$, $E_{\alpha_2-\alpha_S}$ (E_{ij}) vs E_1 correlation plots. The intersection between the horizontal lines at $E_{\alpha_1-\alpha_S}$ or $E_{\alpha_2-\alpha_S} = 3.12$ MeV, $E_{\alpha_1-\alpha_2} = 20.39$ MeV, $E_{\alpha_1-\alpha_2} = 22.3$ MeV and the kinematical curve helps visualizing the region where the 3.03 (green arrows), 20.3 (black

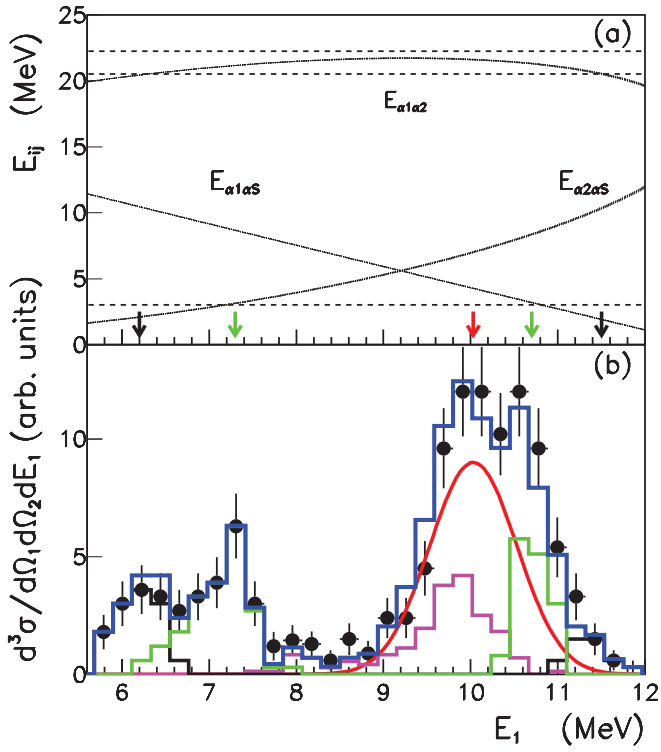

FIG. 5. (Color online) (a) Calculated $E_{\alpha_1-\alpha_2}, E_{\alpha_1-\alpha_S}, E_{\alpha_2-\alpha_S}$ (E_{ij}) vs E_1 correlation plots for (QFR)^p angles $\theta_1 = 109.3^\circ$ and $\theta_3 = 60^\circ$. Dashed horizontal lines at $E_{\alpha_1-\alpha_S}/E_{\alpha_2-\alpha_S} = 3.12$ MeV, $E_{\alpha_1\alpha 2} = 20.39$ MeV, and $E_{\alpha_1\alpha 2} = 22.3$ MeV help visualizing the region where the 3.03 (green arrows) and 20.3 (black arrows) of ^{8}Be give contribution in E_1. The red arrow marks the condition of minimum value for p_S. (b) Corresponding $\alpha - \alpha$ coincidence yield projected onto the E_1 axis (black dots). The blue histogram is the incoherent sum of the QF contribution from (QFR)^p (red line), of the 22.2 (purple line), 20.3 (black line), and 3.03 (green line) MeV levels of ^{8}Be. See text for details.

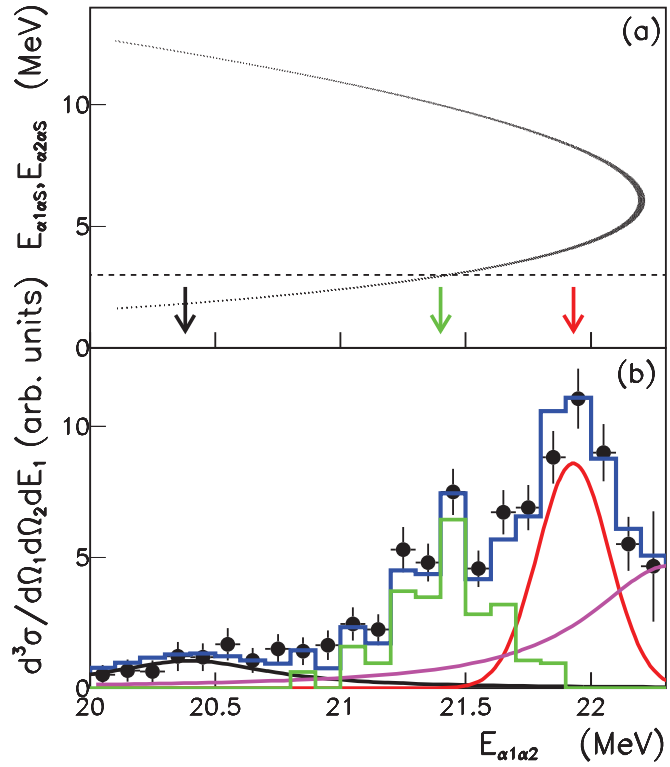

FIG. 6. (Color online) Calculated correlation plots (a) and $\alpha - \alpha$ coincidence yield at the same angles as in Fig. 5 projected onto the $E_{\alpha_1-\alpha_2}$ axis (b). Lines and histograms with the same meaning as in Fig. 5.

arrows), and 22.2 MeV (no intersection, only contribution from the tail) states of ^{8}Be give contribution. The red arrow marks the condition of minimum value for p_S. The blue histogram in the lower part is the incoherent sum of the QF contribution (red line), of the 22.2 (purple line), 20.3 (black line), and 3.03 (green line) MeV levels of ^{8}Be. A good agreement with experimental points is observed, as supported by the following $\tilde{\chi}^2$ values: 0.75 for Fig. 5, 0.62 for Fig. 6, 1.1 for Fig. 7, and 1.07 for Fig. 8. All projected spectra were fitted by assuming a Breit-Wigner shape for the levels involved in the process. The Breit Wigner was drawn in the α-α relative energy variable where there is evidence of resonant behavior. Then a weight function was derived dividing the resulting spectrum by the original one and used to disentangle the SD contribution in the other observables.

1. Momentum distribution in "energy sharing"

QF events thus selected for all pairs of QF angles were then used to reconstruct the experimental p_S distribution of α_S for both (QFR)^p and (QFR)^t inverting the PWIA factorization of Eq. (1). For each pair of QF angles, the three-body coincidence yield was divided by the kinematical factor to obtain the product of the square of the momentum distribution with the HOES two-body cross section. In the restricted angular ranges that localize the QF pairs, the HOES two-body cross section can be considered constant, thus the procedure makes it possible to directly access the momentum distribution [14,17]. The result is shown in Figs. 9 and 10 for the 3.1- and 2.5-MeV runs, respectively [black solid circles for (QFR)^p and empty circles for (QFR)^t], and those figures represent the experimental p_S momentum distribution in arbitrary units in ES. Data were projected with bins of 8 MeV/c (3.1 MeV run) and 13 MeV/c (2.5 MeV run with less statistics) with error bars including statistical errors only. The extracted experimental momentum distributions were then fitted with the theoretical shape (solid line in both figures), given in terms of the Hankel function in momentum space,

$$\Phi(p_S)^2 = \frac{N}{\left(k_S^2 + \beta^2\right)^2}\left[\frac{\sin(k_S R_c)}{k_S} + \frac{\cos(k_S R_c)}{\beta}\right]^2, \quad (5)$$

with $k_S = p_S/\hbar$, R_c the cutoff radius, and $\beta = (2\mu B_{\alpha-d}/\hbar^2)^{1/2}$, where $B_{\alpha-d}$ is the $\alpha - d$ binding energy in ^{6}Li and μ the reduced mass of the system. N and R_c were considered as free parameters and the fit procedure returned $R_c = (6.0 \pm 0.1)$ fm [(5.9 ± 0.3) fm for the 2.5-MeV run] and $N = (7.42 \pm 0.22) \times 10^{-3}$ [$(3.32 \pm 0.17) \times 10^{-3}$ for the 2.5-MeV run]. The theoretical distribution reproduces quite well the shape of the experimental data in both cases, with full widths at half maximum (FWHM) (see Table III), in agreement with the value expected from the literature for the $\alpha - d$ system

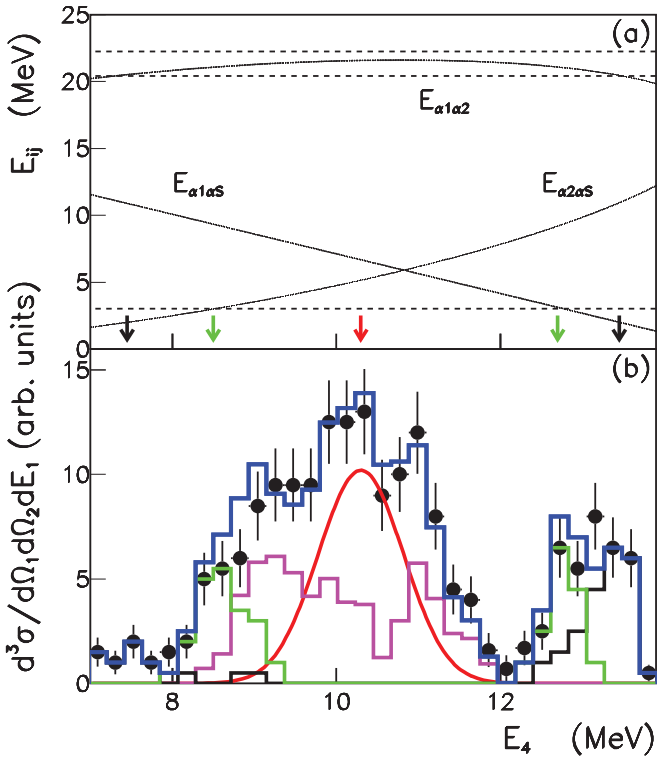

FIG. 7. (Color online) (a) Calculated $E_{\alpha_1-\alpha_2}, E_{\alpha_1-\alpha_S}, E_{\alpha_2-\alpha_S}$ (E_{ij}) vs E_4 correlation plots for $(QFR)^t$ angles $\theta_4 = 86.5^\circ$ and $\theta_2 = 60^\circ$. Dashed horizontal lines at $E_{\alpha_1-\alpha_S}/E_{\alpha_2-\alpha_S} = 3.12$ MeV, $E_{\alpha_1\alpha_2} = 20.39$ MeV, and $E_{\alpha_1\alpha_2} = 22.3$ MeV helps visualizing the region where the 3.03 (green arrows), 20.3 (black arrows), and 22.2 (no intersection, only contribution from the tail) states of ^{8}Be give contribution in E_4. The red arrow marks the condition of minimum value for p_S. (b) Corresponding $\alpha - \alpha$ coincidence yield projected onto the E_4 axis (black dots). The blue histogram is the incoherent sum of the QF contribution from $(QFR)^p$ (red line), of the 22.2 (purple line), 20.3 (black line), and 3.03 (green line) MeV levels of ^{8}Be. See text for details.

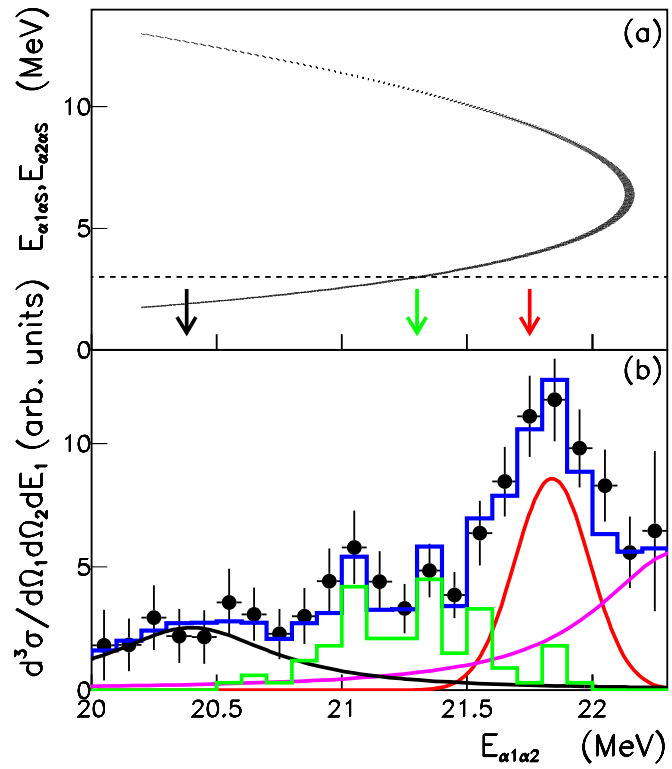

FIG. 8. (Color online) Calculated correlation plots (a) and $\alpha - \alpha$ coincidence yield at the same angles as in Fig. 7 projected onto the $E_{\alpha_1-\alpha_2}$ axis (lb). Lines and histograms with the same meaning as in Fig. 5.

in ^{6}Li [27]. These values are very much consistent within the experimental errors and in agreement with the fact that in the center-of-mass system the two $(QFR)^p$ and $(QFR)^t$ contributions are perfectly indistinguishable.

TABLE III. FWHM from the experimental momentum distributions at 3.1 and 2.5 MeV of beam energy for $(QFR)^p$ and $(QFR)^t$ in ESAC and AC.

Beam energy	Method	QFR	Figure No.	C_{ij}	FWHM (MeV/c)
3.1 MeV	ES	Projectile	9	13	51.2 ± 0.5
3.1 MeV	ES	Target	9	24	51.8 ± 0.5
3.1 MeV	AC	Projectile	13	13	51.6 ± 0.5
3.1 MeV	AC	Target	13	24	51.9 ± 0.5
2.5 MeV	ES	Projectile	10	13	49.5 ± 1.5
2.5 MeV	ES	Target	10	24	49.6 ± 1.5
2.5 MeV	AC	Projectile	14	13	50.1 ± 1.5
2.5 MeV	AC	Target	14	24	50.5 ± 1.5

B. Angular correlation analysis for $(QFR)^p$ and $(QFR)^t$

Another way to test the presence of QF processes is through an AC analysis of the data. Coincidence data were projected onto the E_1 (or E_3) and E_4 (or E_2) energy axes at a fixed angle

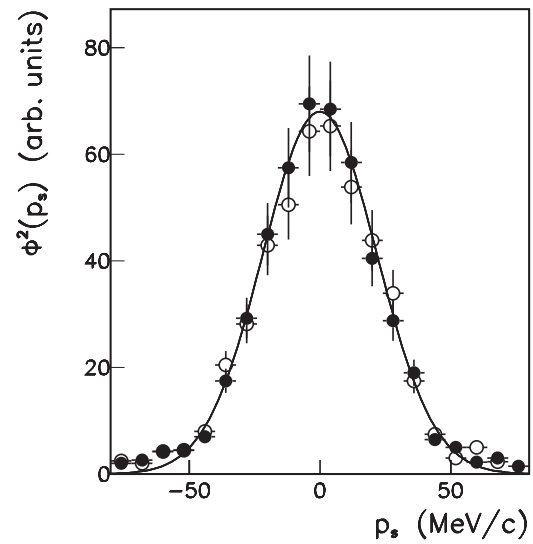

FIG. 9. Experimental momentum distribution for $(QFR)^p$ (black solid circles) and $(QFR)^t$ (empty circles) extracted in ES for the 3.1-MeV run.

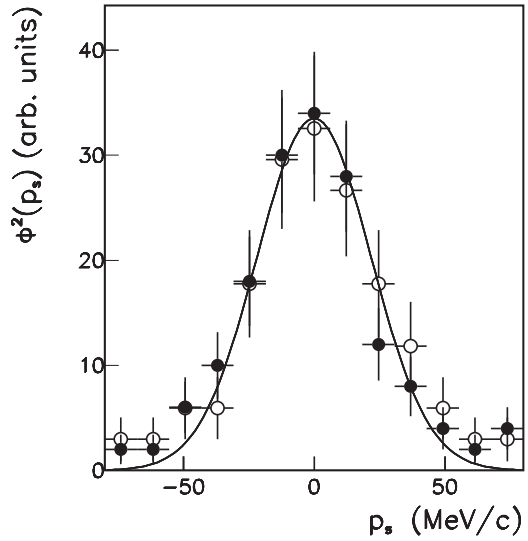

FIG. 10. Experimental momentum distribution for $(QFR)^p$ (black solid circles) and $(QFR)^t$ (empty circles) extracted in ES for the 2.5-MeV run.

θ_3 (θ_2) for one of the two particles and different angles θ_1 (θ_4) for the other particle.

Examples of the resulting projections are reported in Figs. 11 and 12 for θ_3 (θ_2) fixed at $60^\circ \pm 1^\circ$ and different θ_1 (θ_4) spanning the angular range of PSD1 (PSD4).

Typical features appear in the spectra: At the QF angles a broad peak around p_S^{min} is observed (marked with an arrow); the yield of the broad peak is larger at $p_S^{min} = 0$ MeV/c, and decreases while moving away from zero. This reflects the behavior of the p_S distribution that has a maximum for $p_S = 0$ MeV/c, which in turn is from the $l = 0$ relative motion of the $\alpha - d$ system inside ^{6}Li. In general, the presence of SD contributions can make this test much more complicated. However, these features suggest that the QF mechanism is the dominant process in the angular regions close to the QF angles.

1. Momentum distribution in "angular correlation"

The p_S momentum distribution from the AC analysis was obtained projecting the yield at the minimum p_S value for each angular pair, weighted for the weight function of QF processes at the QF angles. The resulting global spectra are reported in Figs. 13 and 14 for the 3.1- and 2.5-MeV run, respectively [black solid circles for $(QFR)^p$ and empty circles for $(QFR)^t$]. Data were projected in 8-MeV/c (3.1-MeV run) and 13-MeV/c bins (2.5-MeV run with less statistics). The error bars account only for statistical errors. The solid lines represent the Hankel function of Eq. (5) with fitting parameters $R_c = (6.0 \pm 0.1)$ fm [(5.9 ± 0.3) fm for the 2.5-MeV run] and $N = (7.21 \pm 0.21) \times 10^{-3}$[$(4.62 \pm 0.23) \times 10^{-3}$ for the 2.5-MeV run]. The FWHM values resulting from the fit are reported in Table III for complete information. These values are very much in agreement with each other and with the values deduced from the ES analysis, providing a very important test of consistency for the present experiment. However, according to [27], we do not expect to have the same FWHM

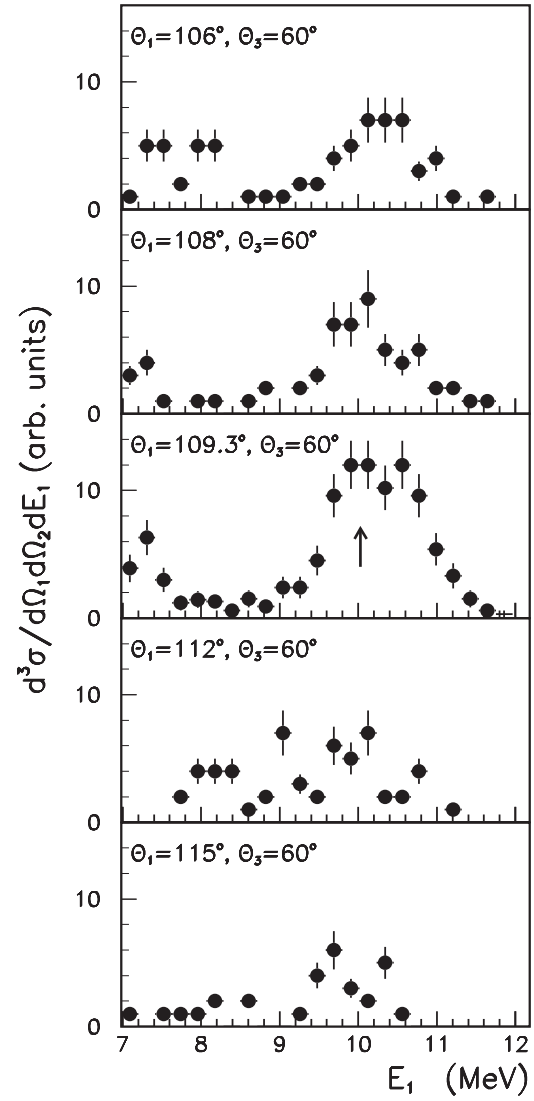

FIG. 11. Typical angular correlation spectra for $(QFR)^p$. The coincidence yield is projected onto the E_1 axis for θ_3 fixed at $60^\circ \pm 1^\circ$ and θ_1 spanning the angular range of PSD1. The condition corresponding to $p_S = 0$ MeV/c is marked with an arrow.

at different beam energies. A change in the beam energy (e.g., in the transferred momentum) modifies the FWHM that increases with increasing beam energy up to its asymptotic value. Nonetheless, the beam energies in the present work provide quite close Galilean invariant transferred momenta (see before) to make the values in Table III all comparable within experimental errors.

C. Investigation of angular regions out of $(QFR)^p$ and $(QFR)^t$

To bring the investigation of QF processes to completion, a cross-check of the kinematical regions far from those of $(QFR)^p$ and $(QFR)^t$ was performed. The ES methodology was applied and typical results are shown in Fig. 15 (energy spectrum in the E_1 variable), and Fig. 16 ($E_{\alpha_1\alpha_2}$ spectrum) at angles $\theta_1 = 100^\circ \pm 1^\circ$ and $\theta_3 = 60^\circ \pm 1^\circ$. As in the previous figures referring to the QF processes, the upper part of

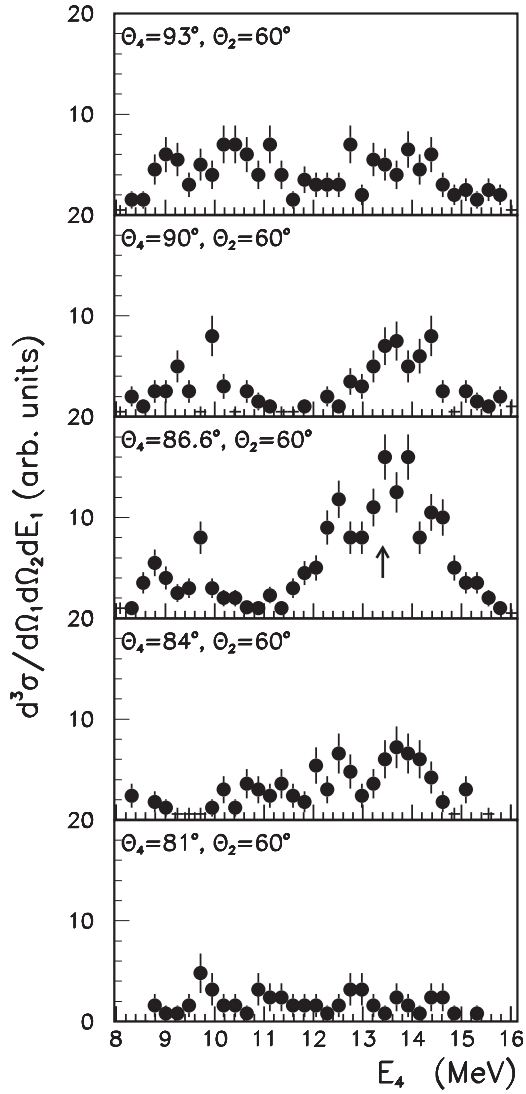

FIG. 12. Typical angular correlation spectra for $(QFR)^t$. The coincidence yield is projected onto the E_4 axis for θ_2 fixed at $60^\circ \pm 1^\circ$ and θ_4 spanning the angular range of PSD4. The condition corresponding to $p_S = 0$ MeV/c is marked with an arrow.

each one-dimensional spectrum shows the calculated $E_{\alpha_1-\alpha_2}$, $E_{\alpha_1-\alpha_S}$, $E_{\alpha_2-\alpha_S}$ (E_{ij}) vs E_1 correlation plots. The intersection with the horizontal line at $E_{\alpha_1\alpha 3}$ or $E_{\alpha_2\alpha 3} = 3.12$ MeV identifies the region where the 3.03 (green arrow) state of ^{8}Be gives contribution. The black arrow shows where the 20.3-MeV state gives contribution. The red arrow marks the condition of minimum value for p_S. The blue histogram in the lower part is the incoherent sum of the several contributions: QF (barely visible red line), 22.2 (purple line) and 3.03 (green line) MeV levels of ^{8}Be. Also in this case a Breit-Wigner shape was used to account for the levels involved in the process in the given angular range. The Breit-Wigner function with correct level parameters was drawn in the relative energy variable where there is evidence of resonant behavior. Dividing the resulting spectrum by the original one gives the weight function to fix each contribution in the other observables. As shown in the figures, energy spectra at these angles are fully

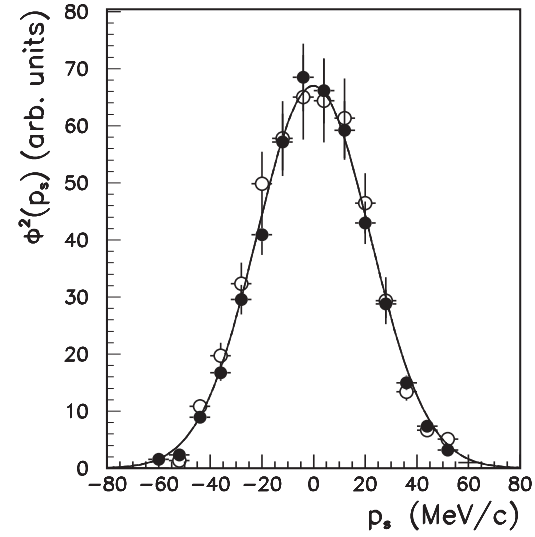

FIG. 13. Experimental momentum distributions for $(QFR)^p$ (black solid circles) and $(QFR)^t$ (empty circles) extracted in AC for the 3.1-MeV run.

dominated by the resonance associated with the 22.2 MeV, $\Gamma = 800$ keV, $J^\pi = 2^+$ level of ^{8}Be. In the $E_{\alpha_1\alpha 2}$ spectrum, the kinematic limit allows only half a resonance to be visible, as already mentioned, while the QF contributions are completely suppressed. The good agreement with experimental points is strengthened by the following $\tilde{\chi}^2$ values: 1.53 for Fig. 15 and 1.56 for Fig. 16.

Thus, some conclusions can be drawn:

(i) At 3.1 and 2.5 MeV of ^{6}Li beam energy, $(QFR)^p$ and $(QFR)^t$ are present and give contribution in the expected kinematical regions. Therefore, the hypothesis of suppression of QF processes is rejected.

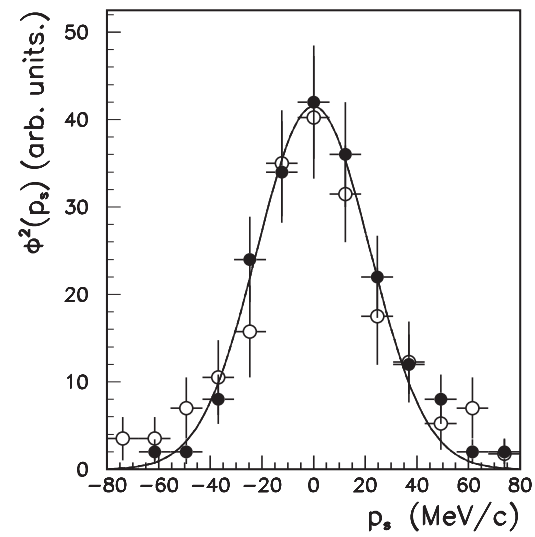

FIG. 14. Experimental momentum distribution for $(QFR)^p$ (black solid circles) and $(QFR)^t$ (empty circles) extracted in AC for the 2.5-MeV run.

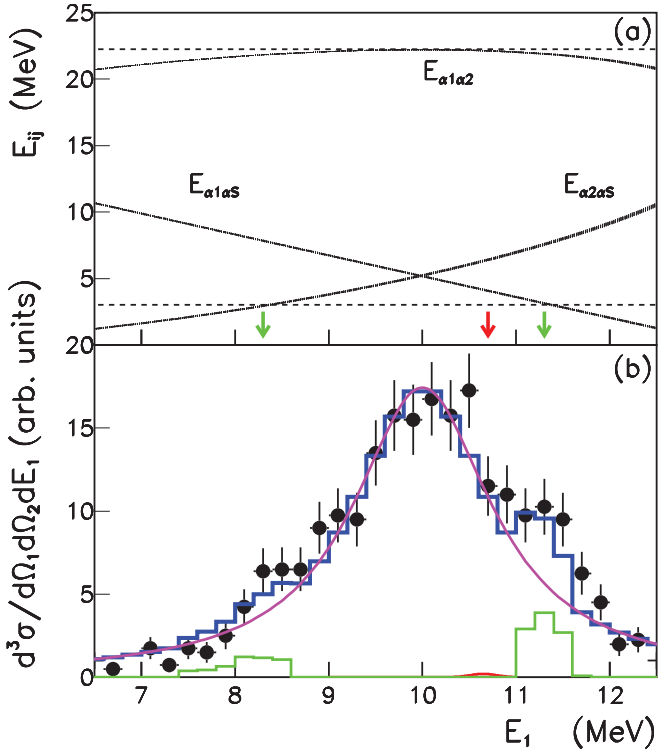

FIG. 15. (Color online) (a) Calculated $E_{\alpha_1-\alpha_2}, E_{\alpha_1-\alpha_S}, E_{\alpha_2-\alpha_S}$ (E_{ij}) vs E_1 correlation plots for angles $\theta_1 = 100$ and $\theta_3 = 60°$. The dashed horizontal line at $E_{\alpha_1-\alpha_S}/E_{\alpha_2-\alpha_S} = 3.12$ MeV helps visualizing the region where the 3.03 (green arrow) state of ^{8}Be gives contribution in E_1. The black arrow indicates the contribution of the 20.3-MeV state of ^{8}Be and the red arrow marks the condition of minimum value for p_S. (b) Corresponding α-α coincidence yield projected onto the E_1 axis (black dots). The blue histogram is the incoherent sum of the QF contribution from $(QFR)^p$ (red line barely visible), of the 22.2 (purple line) and 3.03 (green line) MeV levels of ^{8}Be. See text for details.

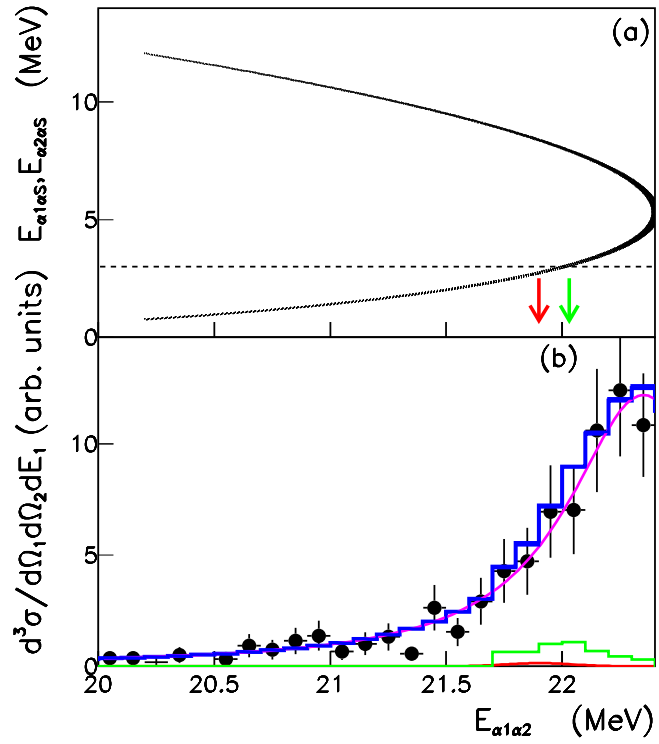

FIG. 16. (Color online) Calculated correlation plots (a) and $\alpha - \alpha$ coincidence yield at the same angles as in Fig. 15 projected onto the $E_{\alpha_1-\alpha_2}$ axis (b). Lines and histograms with the same meaning as in Fig. 15.

(ii) The experimental momentum distributions obtained in ES and AC, whether they refer to $(QFR)^p$ and $(QFR)^t$, are very much in agreement with the experimental errors, confirming for the first time that the two methodologies are absolutely consistent.

(iii) Even at energies lower than the Coulomb barrier the virtual ^{6}Li(d,α)^{4}He process in the ^{6}Li(^{6}Li,$\alpha\alpha$)^{4}He reaction exists and takes place via both $(QFR)^p$ and $(QFR)^t$ mechanisms.

VI. THE α-α ANGULAR CORRELATION SPECTRA

The clear evidence of QF processes from both projectile and target breakup does not allow for further consideration in terms of AQF and the previous interpretation of the huge peak in the α-α angular correlation spectra [10,11] needs to be revised. Here a new interpretation is suggested.

The α-α angular correlation spectra were reconstructed following the procedure reported in Ref. [14]. The coincidence yield to be projected was selected within a center-of-mass energy of α_S of less than 1 MeV, matching with momentum p_3 of the undetected particle parallel and antiparallel to the beam momentum p_0. This provides crossing the kinematical regions corresponding to the two QF processes, because whenever the spectator momentum p_S is zero (either in the target, or in the projectile), p_3 lies in the beam direction.

The coincidence yield was projected onto the emission angle of one of the two detected α particles for a fixed value of the emission angle of the other detected α. Because PSD2 and PSD3 cover the same angles (but from opposite sides), the emission angle was fixed within their angular range. We call this variable $\theta_{\alpha 2}$. In this way we could observe in the same spectrum the behavior of the coincidence yield from both C_{13} and C_{24} coincidences, projecting events corresponding to emission angles of the other α, $\theta_{\alpha 1}$, from 74° to 98° (coincidence C_{24}) and 92° to 121° (coincidence C_{13}).

Results for the 3.1-MeV run are shown in Fig. 17 for three different values of θ_{α_2}: 57°, 60°, and 63° (±1°).

The two side peaks on each figure correspond to $(QFR)^t$ (below 100°) and $(QFR)^p$ (above 100°).

Consistent results were obtained for the 2.5-MeV run.

To give an interpretation of the huge peak in between, the ES analysis was performed in the relevant angular regions. This brings to spectra as those shown in Figs. 15 and 16.

In particular those figures refer to the peculiar condition ($\theta_1 = 100°$, $\theta_3 = 60°$) corresponding to the central value of the huge peak in Fig. 17(b).

From this systematical investigation, it turns out that the huge peak in the α-α angular correlation spectra is nothing but the contribution of the 22.2-MeV resonance.

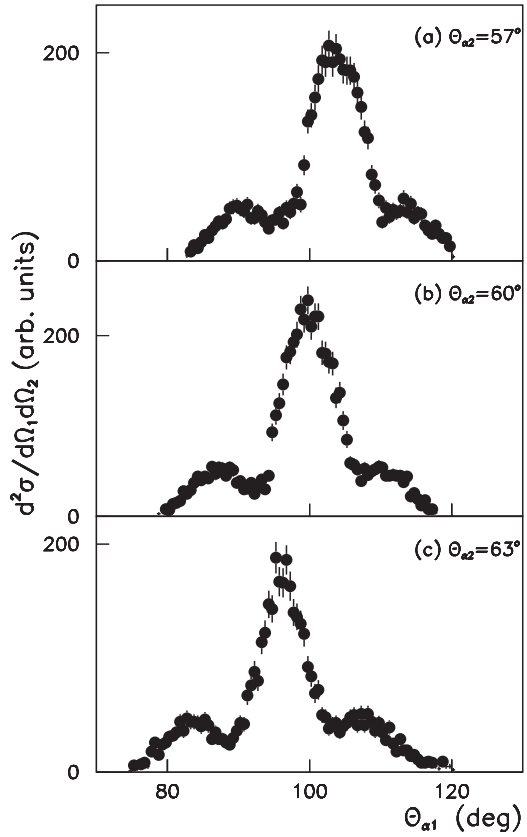

FIG. 17. α-α angular correlation spectra for three different values of $\theta_{\alpha 2}$: (a) 57°, (b) 60°, (c) 63° $\pm$ 1°.

A. Comparison between previous and present α-α angular correlation spectra

The present result was compared with a previous α-α angular correlation spectrum reported in Ref. [14] referring to a measurement at the same beam energy but with a thicker ^{6}Li target (beam energy at half target at 2.4 MeV) and a smaller angular coverage (see [14] for details). Comparison is reported in Fig. 18. Black dots refer to the present experiment, while red ones are from [14].

In spite of the worse resolution and slightly different experimental conditions of the previous experiment, the patterns of the α-α angular correlation spectra are quite consistent with each other, with the presence in both cases of the small peak referring to $(QFR)^t$. The old distribution was normalized to the present one in this region for better comparison.

The other small peak for $(QFR)^p$ is missing in the previous experiment because of the smaller angular range covered in that experiment. However, this evidence was disregarded and only the big central one was for the purpose of discussion at that time and interpreted as clear evidence of the AQF mechanism.

We take advantage of the comparison only to make us sure of the reproducibility of the experimental spectrum for which we have provided here a totally different interpretation.

B. New interpretation of the α-α angular correlation spectra

Here we provide a different interpretation also for the so-called characteristic feature of both single and coincidence

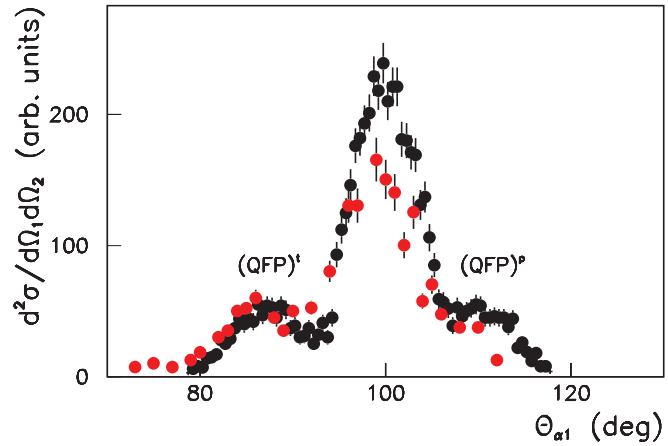

FIG. 18. (Color online) α-α angular correlation spectrum at θ_2 = 60° $\pm$ 1°: comparison between present experiment (black dots as in Fig. 17(b), and the one from [14] at nearly the same energy (red dots).

angular correlation α spectra, in the energy range $E_{^6\mathrm{Li}}$ = 3−7 MeV, namely the transition from two to one huge peak that can be clearly observed in Ref. [14] and wrongly assigned to the disappearance of the QF processes in favor of the AQF one. We make use of a 2D spectrum θ_{α_1} vs E_{α_2} for fixed θ_{α_2} = 60° ($\pm$1°) reported in Fig. 19.

Colored regions on top of the coincidence yield represent simulated loci referring to $E_{\alpha_1\alpha_2}$ = 22.3 MeV at the same kinematical conditions and for ^{6}Li beam energies of 2.7 (purple), corresponding to 3.1 MeV of beam energy at half target, 3.2 (blue), 3.6 (red), and 4.7 (green).

These loci represent the phase space regions where the 22.2-MeV state of ^{8}Be might give contribution. For clearness, each colored area was reduced with respect to the real extent corresponding to the 800-keV width of the ^{8} Be level. It shows up that while at the energy of the present experiment (3.1 MeV), its contribution is concentrated in a small region that gives a peak when projected in the θ_{α_1} variable; at higher

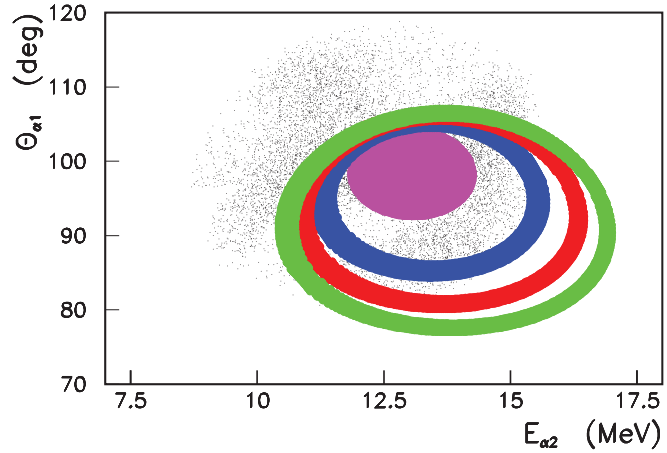

FIG. 19. (Color online) 2D spectrum θ_1 (θ_4) vs E_3 (E_2) at θ_3(θ_2)= 60° ($\pm$1°). Colored regions on top of the coincidence yield represent simulated loci referring to $E_{\alpha_1\alpha_2}$ = 22.3 MeV for ^{6}Li beam energies of 2.7 (purple), 3.2 (blue), 3.6 (red), and 4.7 (green).

beam energy its appearance is spread over a wider range of θ_{α_1}, contributing in the two-peak pattern shown in Fig. 4 of Ref. [14].

Thus, the two- to one-peak transition is nothing but a phase space effect connected with the feeding of the 22.2-MeV level of ^{8}Be.

The same arguments hold for the 2.5-MeV run, whose coincidence events give contribution inside the purple region.

VII. CONCLUSIONS

The $^6\mathrm{Li} + {}^6\mathrm{Li} \rightarrow 3\alpha$ reaction was measured at incident energies of 3.1 and 2.5 MeV well below the Coulomb barrier to probe the existence of QF mechanisms even below the barrier. In earlier experimental studies at near the same energy these mechanisms were thought to merge in the AQF mechanism that takes place after the two ^{6}Li relative motion is brought to rest by the Coulomb repulsion. Such invoked direct process assumes the breakup of both ^{6}Li nuclei, which is far from being likely if no energy is left for the interaction after the Coulomb slowing down.

On the other hand, it was never justified why QF processes should take place only at rest rather than at any intermediate relative velocity as a consequence of the Coulomb slowing down for energies around the barrier. The high resolution of the present experiment has made possible a clearer and more careful analysis of the experimental results than before showing the unambiguous appearance of QF mechanisms in the kinematical regions where expected. Coincidence data have been analyzed in ES and AC providing very consistent results for both $(\mathrm{QFR})^p$ and $(\mathrm{QFR})^t$. Thus, we can conclude that the distinctive condition for the QF mechanism to be present is not the beam energy but the transferred momentum q_t from nucleus A to nucleus $B = C + D$. This is the Galilean invariant transferred momentum of Ref. [27], strongly connected to the Q value of the given nuclear process.

As for the huge peak in the α-α angular correlation spectrum, previously ascribed to the AQF process, a more reliable interpretation is here provided. From a very detailed analysis it turns out that the peak is from the contribution of the very large ($\Gamma = 800$ keV) 22.2-MeV level of ^{8}Be, resulting thus in a correction of earlier interpretations claiming that no single hypothesis could be drawn based upon decay states of ^{8}Be. A new experiment of the $^6\mathrm{Li} + {}^6\mathrm{Li} \rightarrow 3\alpha$ reaction at lower energy is foreseen to investigate the behavior of QF processes in a clearer condition, free of the contribution of the 22.2-MeV level of ^{8}Be.

ACKNOWLEDGMENTS

The authors would like to thank Professor S. Cherubini, Professor A. Musumarra, and Dr. M. G. Pellegriti for their valuable help during the experiment. This work was partially supported by the Italian Ministry of University (MIUR) under grant LNS-Astrofisica Nucleare (fondi premiali).

[1] M. N. Huberman, M. Kamegai, and G. C. Morrison, Phys. Rev. **129**, 791 (1963).
[2] M. Kamegai, Phys. Rev. **131**, 1701 (1963).
[3] J. M. Coste and L. Marquez, Nucl. Phys. **54**, 257 (1964).
[4] A. Garin, C. Lemeille, D. Manesse, L. Marquez, and N. Saunier, Journ. Phys. (Paris). **25**, 768 (1964).
[5] J. H. Shafer, Phys. Rev. **133**, B920 (1964).
[6] E. H. Berkowitz, Nucl. Phys. **82**, 52 (1966).
[7] B. Frois, L. Marquez, J. L. Quebert, J. N. Scheurer, G. Gruber, E. Heinicke, and K. Meier-Ewert, Nucl. Phys. A **153**, 277 (1970).
[8] L. L. Gadeken and E. Norbeck, Phys. Rev. C **6**, 1172 (1972).
[9] R. E. Warner, C. Ball, W. G. Davies, and A. J. Ferguson, Nucl. Phys. A **341**, 483 (1980).
[10] E. Norbeck, C. R. Chen, M. D. Strathman, and D. A. Fox, Phys. Rev. C **23**, 2557 (1981).
[11] M. Lattuada, F. Riggi, C. Spitaleri, D. Vinciguerra, and C. M. Sutera, Phys. Rev. C **26**, 1330 (1982).
[12] M. Lattuada, F. Riggi, C. Spitaleri, D. Vinciguerra, G. Vourvopulos, X. Aslanoglou, and Đ. Miljanić, Phys. Rev. C **30**, 531 (1984).
[13] M. Lattuada, F. Riggi, D. Vinciguerra, C. Spitaleri, and Đ. Miljanić, Z. Phys. A-Atomic Nuclei **328**, 497 (1987).
[14] M. Lattuada, F. Riggi, D. Vinciguerra, C. Spitaleri, G. Vourvopulos, and Đ. Miljanić, Z. Phys. A-Atomic Nuclei **330**, 183 (1988).
[15] C. Spitaleri, in *Problems of Fundamental Modern Physics II: Proceedings*, edited by R. Cherubini, P. Dalpiaz, and B. Minetti (World Scientific, Singapore, 1990), p. 21.
[16] S. Cherubini, V. N. Kondratyev, M. Lattuada, C. Spitaleri, Đ. Miljanić, M. Zadro, and G. Baur, Astrophys. Journ. **456**, 855 (1996).
[17] C. Spitaleri, S. Typel, R. G. Pizzone, M. Aliotta, S. Blagus, M. Bogovac, S. Cherubini, P. Figuera, M. Lattuada, M. Milin, Đ. Miljanić, A. Musumarra, M. G. Pellegriti, D. Rendic, C. Rolfs, S. Romano, N. Soic, A. Tumino, H. H. Wolter, and M. Zadro, Phys. Rev. C **63**, 055801 (2001).
[18] A. Musumarra, R. G. Pizzone, S. Blagus, M. Bogovac, F. Figuera, M. Lattuada, M. Milin, Đ. Miljanić, M. G. Pellegriti, D. Rendic, C. Rolfs, N. Soic, C. Spitaleri, S. Typel, H. H. Wolter, and M. Zadro, Phys. Rev. C **64**, 068801 (2001).
[19] C. Spitaleri, S. Cherubini, A. Di Pietro, P. Figuera, M. Gulino, M. Lattuada, Đ. Miljanić, A. Musumarra, M. G. Pellegriti, R. G. Pizzone, C. Rolfs, S. Romano, S. Tudisco, and A. Tumino, Nucl. Phys. A **719**, C99 (2003).
[20] C. Spitaleri, A. M. Mukhamedzhanov, L. D. Blokhintsev, M. La Cognata, R. G. Pizzone, and A. Tumino, Phys. Atom. Nucl. **74**, 1725 (2011).
[21] C.Spitaleri, in *From the Big Bang to the Nucleosynthesis, International School of Physics "Enrico Fermi", Course CLXXVIII*, edited by A. Bracco and E. Nappi (IOS, Amsterdam; SIF, Bologna, 2011), p. 210.
[22] R. E. Tribble, C. A. Bertulani, M. La Cognata, A. M. Mukhamedzhanov, and C. Spitaleri, Rep. Prog. Phys. **77**, 106901 (2014).
[23] I. S. Shapiro, V. M. Kolybasov, and R. Augst, Nucl. Phys. A **61**, 353 (1965).

[24] I. S. Shapiro, Sov. Physics Uspekhi **10**, 515 (1968).
[25] I. S. Shapiro, in *Interaction of High-Energy Particles with Nuclei, International School of Physics "Enrico Fermi", Course XXXVIII*, edited by E. Ericson (Academic Press, New York, 1967), p. 210.
[26] G. F. Chew and G. C. Wick, Phys. Rev. **85**, 636 (1952).
[27] R. G. Pizzone, C. Spitaleri, S. Cherubini, M. La Cognata, L. Lamia, Đ. Miljanić, A. Musumarra, S. Romano, A. Tumino, S. Tudisco, and S. Typel, Phys. Rev. C **71**, 058801 (2005).
[28] S. Barbarino, M. Lattuada, F. Riggi, C. Spitaleri, and D. Vinciguerra, Phys. Rev. C **21**, 1104 (1980).
[29] R. G. Pizzone, C. Spitaleri, A. M. Mukhamedzhanov, L. D. Blokhintsev, C. A. Bertulani, B. Irgaziev, M. La Cognata, L. Lamia, and S. Romano, Phys. Rev. C **80**, 025807 (2009).
[30] J. Kasagi, T. Nakagawa, N. Sekune, T. Tohei, and H. Ueno, Nucl. Phys. A **239**, 233 (1975).